INVESTIGATING THE DAMAGE-TOLERANT DESIGN OF STIFFENER RUN-OUTS

S.Psarras[1*], S.T.Pinho[1], B.G.Falzon[2]

[1] *Dept. Aeronautics, Imperial College London, SW7 2AZ, United Kingdom*
[2] *Dept. Mechanical and Aerospace Engineering, Monash University, Victoria, 3800, Australia*
** s.psarras07@imperial.ac.uk*

Keywords: A. Carbon fibre; B. Damage tolerance; C. Finite element analysis (FEA); D. Acoustic emission

Abstract
In this work, the use of a compliant web design for improved damage tolerance in stiffener run-outs is investigated. Three different configurations were compared to establish the merits of a compliant design: a baseline configuration, a configuration with optimised tapering and a compliant configuration. The performance of these configurations, in terms of strength and damage tolerance, was compared numerically using a parametric finite element analysis. The energy release rates for debonding and delamination, for different crack lengths across the specimen width, were used for this comparison. The three configurations were subsequently manufactured and tested. In order to monitor the failure process, Acoustic Emission (AE) equipment was used and proved valuable in the detection and analysis of failure. The predicted failure loads, based on the energy release rates, showed good accuracy, particularly when the distribution of the energy release rate across the width of the specimen was taken into account. As expected, the compliant configuration failed by debonding and showed improved damage tolerance compared to the baseline and tapered stiffener run-outs.

1 Introduction

Modern aerostructures are predominantly of semi-monocoque construction characterized by a thin skin and stiffeners. The latest generation of large passenger aircraft also use mostly carbon-fibre composite material in their primary structure and there is a trend towards the utilization of bonding of subcomponents in preference of mechanical fastening. Current design philosophy requires that certain stiffeners are terminated, for example due to an intersecting structural feature or an inspection cut-out. In these circumstances, the loading in the stiffener must be diffused into the skin, leading to complex three-dimensional stress-states. The development and utilization of reliable virtual component testing, in the design of composite aerostructures, can potentially yield significant cost reductions. Such reliability requires a thorough understanding of the damage mechanisms and failure processes in realistic aerostructures, particularly in critical regions such as stiffener run-outs.

When a stiffener is terminated, the loads which it carries must be transferred to the skin, making the design of the run-out region vital; hence, improved design methodologies are

required. Several studies of skin-stiffener failure [1-8] have been carried out. Falzon et al. [7, 8] investigated the failure of realistic stiffener run-outs loaded in uniaxial compression. Different stacking sequences and skin thicknesses at the run-out region were tested and a wealth of complexity in the response and subsequent failure was reported. For all tests, failure initiated at the edge of the run-out and propagated across the skin–stiffener interface. It was found that the failure load of each specimen was greatly influenced by changes in the geometric features of these specimens. Falzon and Hitchings [8] used a Virtual Crack Closure Technique (VCCT) [9] to predict the crack growth characteristics of the modelled specimens and reported shortcomings in the quantitative correlation between the predicted and observed failure loads and modes. Bisagni et al. [10] investigated, experimentally and numerically, the postbuckling response of hat-stiffened composite panels using cohesive zone models and predicted collapse loads which were in agreement with experiments. Krueger [6] used VCCT and a numerically effective shell/3D modelling approach to predict the delamination failure of skin-stiffener run-outs. Camanho et al. [11] implemented a cohesive element to numerically investigate the debond strength of skin-stiffener composite specimens using cohesive zone models and compared with experimental results.

In a recent study by the authors [12], a parametric numerical analysis was conducted to optimize the design of the run-out section to increase the crack growth stability under axial compression. Improved damage tolerance (stable crack propagation) was reported in the modified stiffener run-out design as compared to the baseline configuration. The modified design eventually failed catastrophically by interlaminar delamination, not bondline failure, which had not been considered in the numerical study. A more detailed analysis of different configurations, which accounts for delamination, was therefore undertaken in this paper. Building on the previous findings, the merits of a compliant termination scheme are presented.

The research in this paper focuses on stiffener run-outs loaded in compression with a selection of compliant stiffener termination schemes. These schemes are analysed numerically (Section 2) in order to compare the influence of the design on the energy release rates for debonding and delamination. The stiffener run-outs were manufactured and tested to failure (Section 3). The experimental results are presented in Section 4, and compared to the predictions in Section 5.

2 Numerical Analysis

2.1. Skin-stiffener configurations

The main focus of this study was on developing a new stiffener run-out configuration with improved crack growth stability and a higher debond strength. Four new configurations were analyzed, Figure 1. The first design, *Compliant 1*, is a stiffener run-out tapered down to the edge, in order to remove the geometric discontinuity, with a widening in the flange to avoid delamination. Another approach, *Compliant 2*, had a 45^o notch cut at the base of the stiffener which was filled with an adhesive spew fillet. The insertion of the adhesive at the base was used in order to reduce the local peeling stresses. Two more designs were developed by considering the potential benefits of local stiffness variations; one with a step tapered blade, *Compliant 3*, and the other with a curved cut, *Compliant 4*. Compared to the *Baseline* stiffener (Figure 4a), all proposed configurations have a widening flange towards the termination end of the stiffener but this added material is offset by the taper of the stiffener web. This results in stiffener design with similar overall weight to the *Baseline* designs.

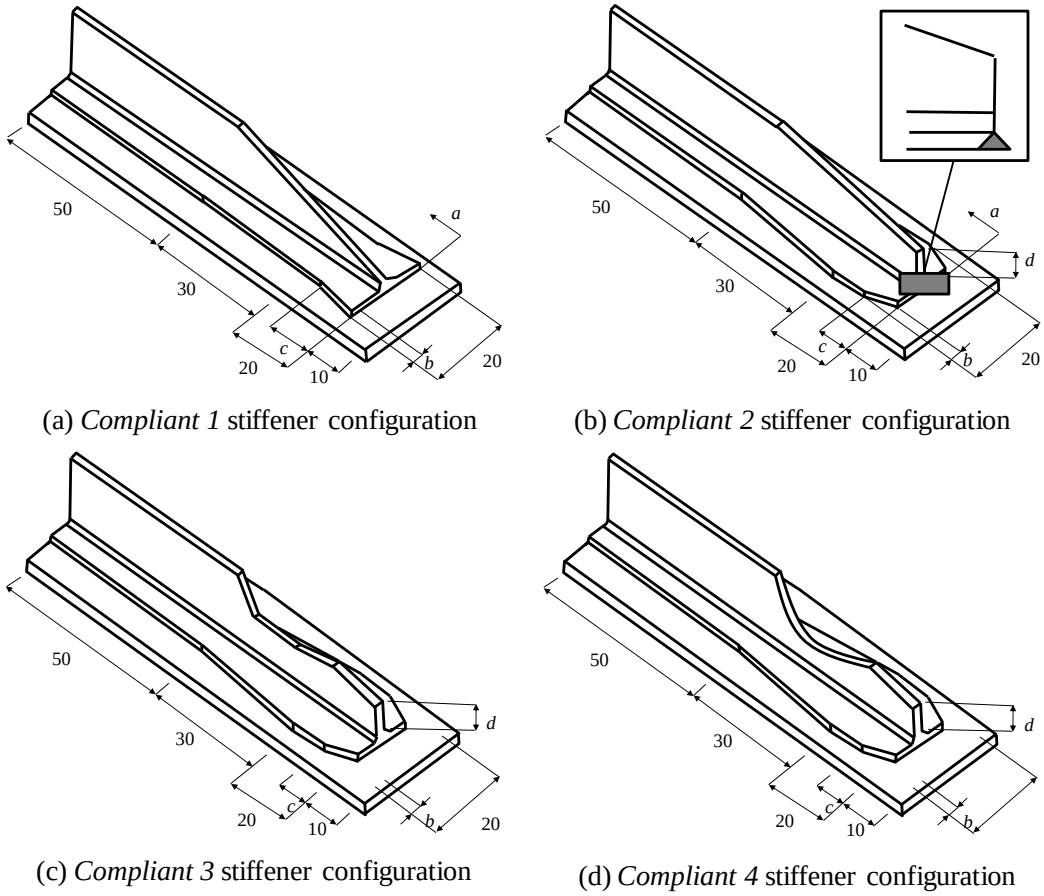

(a) *Compliant 1* stiffener configuration (b) *Compliant 2* stiffener configuration

(c) *Compliant 3* stiffener configuration (d) *Compliant 4* stiffener configuration

Figure 1. The *Compliant* designs

2.2. Finite element models

All the finite element (FE) simulations of the parametric study were carried out in the FE package Abaqus/Standard [13] and the parameterized models were created using the scripting language Python [14]. The model had six different parts, the skin, the adhesive between the skin and the stiffener, the 2 parts of the stiffener, the delamination part, and the filler. The materials used in this study were IM7/8552 carbon/epoxy pre-preg, with ply thickness 0.25 mm, for the skin and the stiffener, and FM300 adhesive film (0.15 mm thick) for the bondline. The material properties for IM7/8552 measured using standard tests are shown in Table 1. The FE model with boundary conditions is shown in Figure 2c.

Material	E_{xx} **[GPa]**	E_{yy} **[GPa]**	G_{xy} **[GPa]**	ν_{xy}	X **[MPa]**	Y **[MPa]**	S **[MPa]**	G_{Ic} **[kJ/m^2]**	G_{IIc} **[kJ/m^2]**	n
IM7/8552	154.1	9.8	4.48	0.34	1572.9	254.6	101.2	0.21	0.61	-
FM300	2.38	-	0.68	-	61	-	49.8	0.9	2.5	8.0

Table 1: Material properties for IM7/8552, measured in-house, and FM300

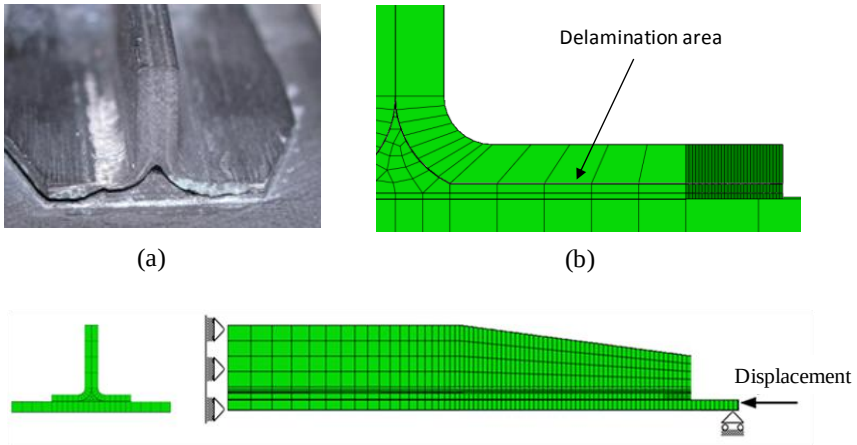

Figure 2. a) *Tapered* stiffener after testing, b) FE model showing delamination path, and c) FE model of a specimen with boundary conditions.

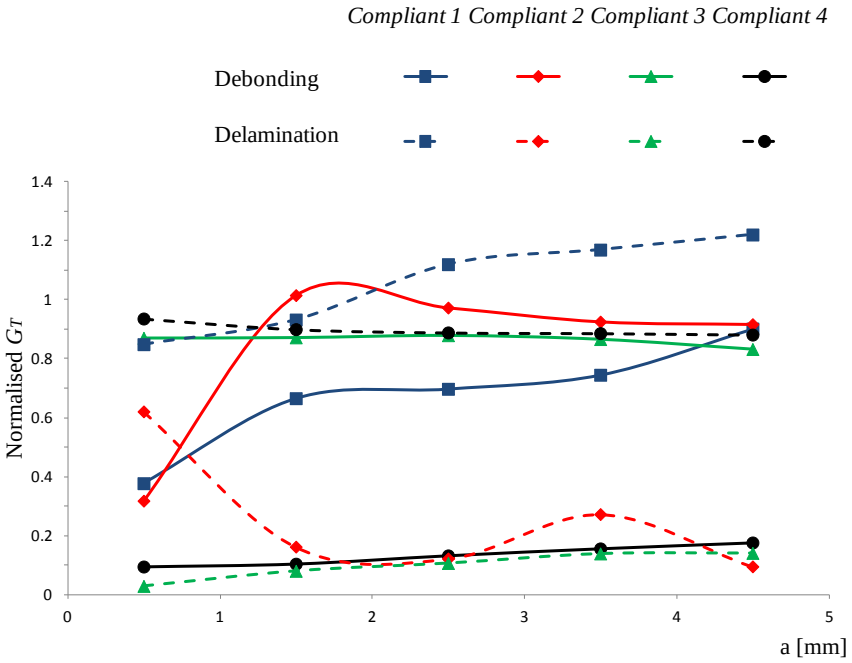

Figure 3 Normalized strain energy release rates as a function of crack length; comparison between *Compliant* designs

The different configurations in this study were assessed by comparing the energy release rates of the run-outs for a given end displacement and for several initial debond lengths, following the procedure described in a previous study [12]. The results of the normalised strain energy release rates of the *Compliant* designs are shown in Figure 3, where the values of $G_T = G_I + G_{II} + G_{III}$, the total strain energy release rate, have been normalized by the G_T of the reference parametric stiffener for 0.5 mm of crack length. The negative slope of the *G(a)* curve indicates crack growth stability, while a positive slope indicates instability (assuming constant fracture toughness). From a comparison of the four designs, it can be assumed that the best performance is expected from the *Compliant 4* design.

2.3. Energy release rate along crack

The structural performance of three different skin-stiffener configurations – *Baseline* (B), *Tapered* (T) and *Compliant* (C) – under longitudinal compression, with geometry and dimensions shown in Figure 4, was assessed.

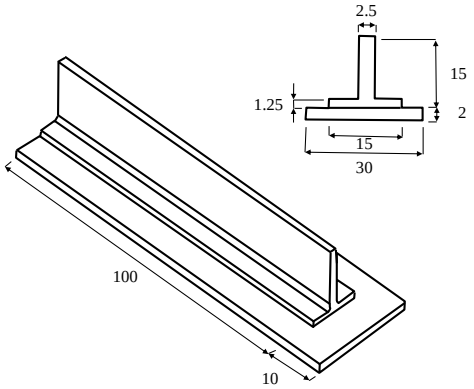

(a) *Baseline* stiffener configuration

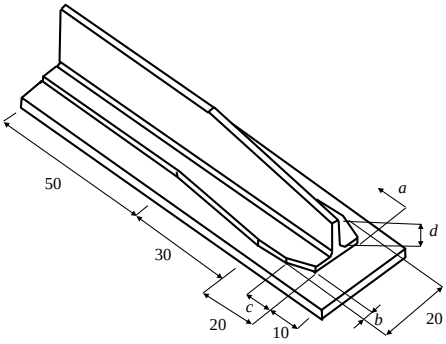

(b) *Tapered* stiffener configuration

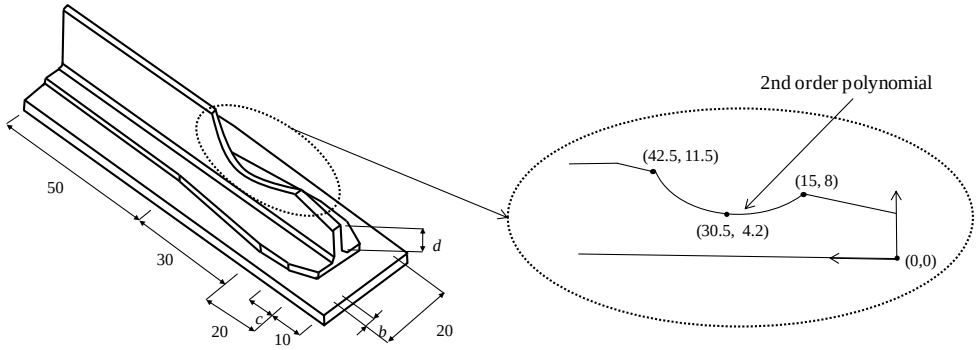

(c) *Compliant* stiffener configuration

Figure 4. Stiffener design configurations (dimensions in mm).

Note that the *Compliant* design is the *Compliant 4* design from Figure 1 which exhibited the best structural performance from the compliant designs tested. The three different configurations, *Baseline*, *Tapered* and *Compliant* (see Figure 4), were analysed for debonding and delamination growth stability. The results of this analysis are presented in Figure 5.

Figure 5 compares the normalised strain energy release rate for the *Baseline*, the *Tapered* and the *Compliant* stiffeners. Recalling the failure modes obtained experimentally [12], the *Baseline* stiffener failed by debonding and the *Tapered* stiffener initially experienced debonding until it finally failed by delamination. This is in agreement with the predictions in Figure 5. Consequently, both models were able to correctly describe these experimental results [12]. In addition, the stability analysis for the *Compliant* stiffener predicts that this design will fail stably by debonding, Figure 5.

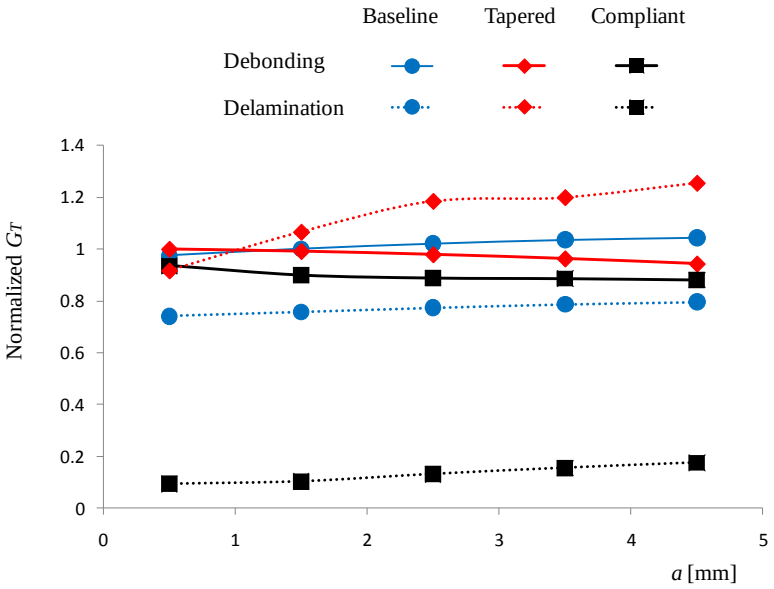

Figure 5. Normalized strain energy release rates as a function of crack length; comparison between *Baseline* stiffener design (Figure 4a), *Tapered* stiffener (Figure 4b) and *Compliant* stiffener (Figure 4c) with dimensions (see Figure 4c) b=3 mm, c=10 mm and d=6.25 mm.

2.4. Energy release rate along the width of the crack tip

The strain energy release rate along the width of the crack tip was calculated for the *Baseline*, *Tapered* and *Compliant* configurations (Figure 6). Fracture initiation is expected when the G_T exceeds the fracture toughness G_c for a given mixed-mode ratio G_{II} / G_T at each point along the crack tip. In other words, propagation at each point occurs when G_T / G_c >1 [15, 16]. The interlaminar fracture toughness, G_c, can be calculated by using the following equation[16]:

$$G_c = G_{Ic} + (G_{IIc} - G_{Ic})\left(\frac{G_{IIc}}{G_T}\right)^{\eta} \tag{1}$$

where G_{Ic} and G_{IIc} are the experimental values of fracture toughness for mode I and II and η is determined by curve fitting (see Table 1). The value of G_c is normalised to the width-average value for the *Tapered* specimen. It can be observed in Figure 6 that the trend is similar for the *Baseline* and *Tapered* specimen types but is different in the centre of the *Compliant* stiffener. This is due the difference in the web of the stiffeners. The curved taper has reduced the normalized strain energy release rate in the centre without affecting the trend in the flange. The maximum value of the energy release rate can be used to predict the load corresponding to the initiation of fracture using

$$\frac{P}{P_{FE}} = \sqrt{\frac{G_c}{G_T}} \tag{2}$$

where P is the load at initiation of fracture, P_{FE} is the load from the FE model, G_c the critical strain energy release rate (Equation 1), and G_T is the strain energy release rate predicted by

the FE model as defined previously. Two different predictions for P can be made: one using the maximum value of G_T along the width, and another using the average.

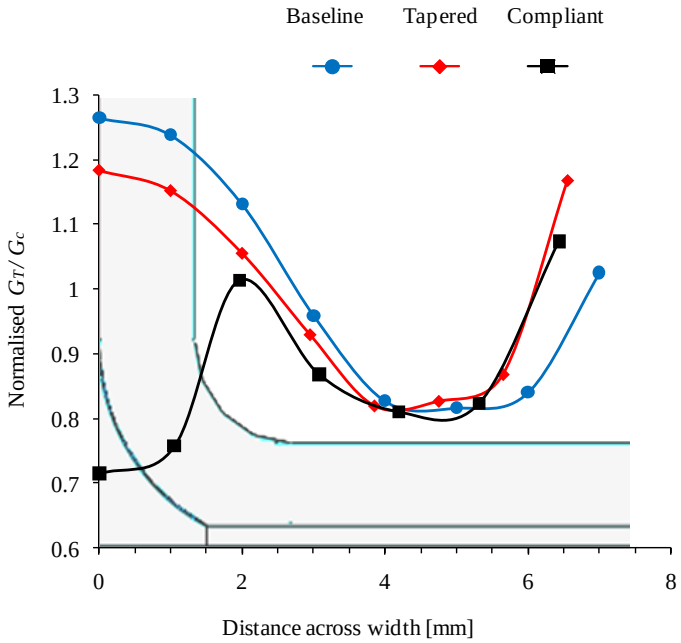

Figure 6. Normalized G_T/G_c across the crack tip for crack a = 1 mm for the *Baseline*, *Tapered* and *Compliant* specimens.

3 Experiments

The tests were carried out in an Instron testing machine, equipped with a 100 KN load cell, at a loading rate of 0.5 mm/min. Load and crosshead displacement were recorded continuously by a PC data logger connected to the load cell and the Instron machine at a sampling rate of 2 Hz. The specimens were aligned by careful measurement in the loading direction to avoid bending. Because the specimens were machined before in a way that the ends of the pots were parallel and the skin of the stiffener perpendicular, it was ensured the specimen's skin was centred in the load cell. The Imperial Data Acquisition (IDA) program was used to record load and displacement during the tests. Also a high resolution camera, Canon EOS 20 Megapixel, was taken photos periodically in order to detect any surface damage and debonding.

AE sensors were used to identify and investigate failures inside the specimens during testing. The AE equipment was manufactured by Physical Acoustic Corporation (PAC) and failure was monitored by AEwin software. Broadband (WD) sensors with an operating frequency range of 100 Hz to 1000 kHz were used and positioned in order to obtain the best results without affecting the specimens behaviour. The classification of the failure modes generated after AE signals collected from a range of standard tensile tests of various ply orientations and then recognized in other specimens where more complex failure processes take place [17].

4 Results

The *Baseline* stiffeners had an average failure load of 16.5 kN while the *Tapered* stiffeners had an average failure load of 17.7 kN and the *Compliant* stiffeners an average failure load of 18 kN, Table 2. The fracture surfaces for selected specimens are shown in Figure 7, and the load versus displacement curves for selected specimens of the three stiffener designs are

shown in Figure 8. The predicted loads (using Eq. 2) match well with the experimental values when the maximum *G* across the width is used, Table 2.

	Predicted failure load [kN] (% difference with respect to experimental)		**Experimental failure load [kN]**
	Based on G_{avg}	Based on G_{max}	
***Baseline* Stiffener**	19.00 (+15.2%)	16.56 (+0.4%)	$16.49^{+0.34}_{-0.39}$
***Tapered* Stiffener**	19.17 (+8.2%)	17.45 (-1.5%)	$17.72^{+0.16}_{-0.22}$
***Compliant* Stiffener**	19.93 (+10.6%)	18.17 (+0.8%)	$18.02^{+0.16}_{-0.29}$

Table 2: Failure loads for the different specimen types, as well as the predicted failure loads using Eq. 2.

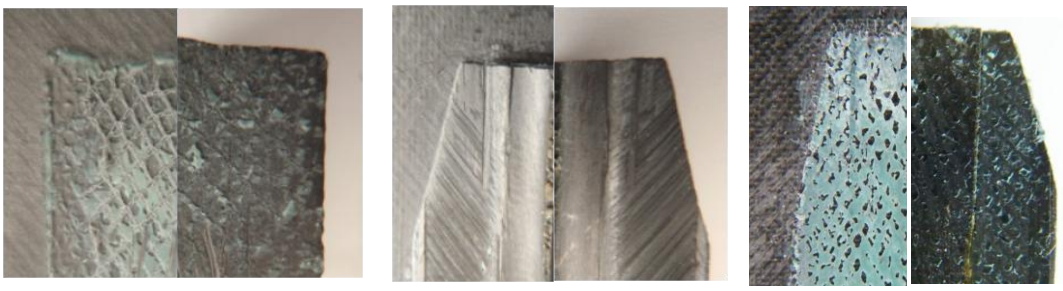

(a) (b) (c)

Figure 7. a) *Baseline* stiffener, (b) *Tapered* Stiffener and (c) *Compliant* Stiffener after failure respectively.

The acoustic emission signals (Figure 8) show that there was an increase in AE activity 0.01 mm before catastrophic failure for the *Baseline* specimen. This activity corresponds mostly to delamination and matrix cracking according to the signal classification. For the *Tapered* specimen type, the increase in AE emission started about 0.05 mm before catastrophic failure but more peak frequencies in fibre/matrix debonding, which is in line with the experiments. The *Compliant* specimen had an increase in the AE activity 0.1 mm before the final failure only in matrix cacking band. Figure 8 also shows the peak frequency during the tests for all specimen types. It can be observed that there is some very low-energy micro-cracking from the start of the test and this is possibly at the resin pots. The *Tapered* specimen configuration promoted a combination of failure modes including delamination and fibre bridging which preceded catastrophic failure. In addition, the *Compliant* stiffener, according to AE data and as visually observed (Figure 7c), suffered only from debonding.

5 Discussion

The strain energy release rate analysis yielded good results in the investigation of the run-out design influence in debonding/delamination for stiffener terminations. The FE models accurately predicted the failure loads and failure modes for the specimens tested and the predictions were improved when the distributions of the strain energy release rate across the width was considered. The differences in the predictions using the average and the maximum energy release rates are shown in Table 2 and can be compared to the experimental failure loads. The load-displacement, as well as the peak frequency-displacement plots (Figure 8),

show that the *Tapered* design is slightly more damage tolerant than the *Baseline* one and this improved further with the *Compliant* design. The AE monitoring proved to be valuable in detecting and analysing the failure modes experienced by the specimens.

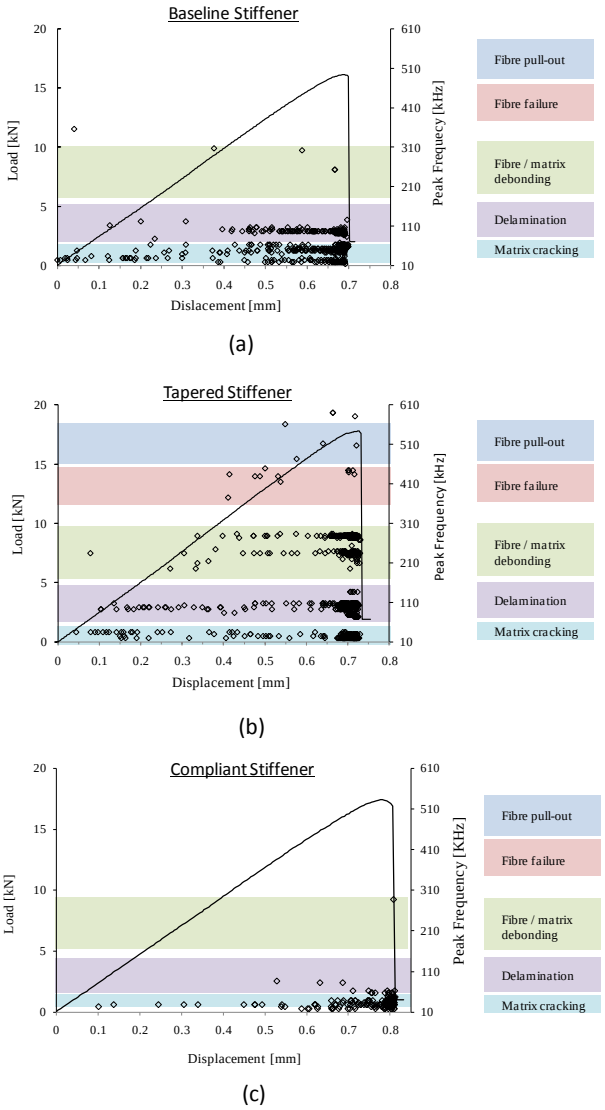

Figure 8. Loads and Peak frequencies versus displacement for a) the *Baseline* b) the *Tapered* and c) the *Compliant* stiffeners. A scale on the right hand side indicates the mode of failure typically associated with these peak frequencies [17].

6 Conclusions

This study was based on the strain energy release rates for debonding and delamination and successfully predicted the failure loads for the three different specimen types. The predictions were more accurate when the maximum strain energy release rate across the width was used. It can be concluded that the variation of the energy release rate across the width should be considered when stiffener run-outs are designed. AE data recorded during skin-stiffener run-out compression tests proved useful to analyse the failure processes which take place in these specimens. The results show that in the design of skin-stiffener run-outs it is important to consider the possibility of failure modes other than debonding, and that compliant termination schemes offer the possibility of improved damage tolerance.

REFERENCES

1. Faggiani, A. and B.G. Falzon, *Numerical analysis of stiffener run-out sections.* Applied Composite Materials, 2007. **14**(2): p. 145-58.
2. Falzon, B.G., K.A. Stevens, and G.O. Davies, *Postbuckling behaviour of a blade-stiffened composite panel loaded in uniaxial compression.* Composites Part A (Applied Science and Manufacturing), 2000. **31A**(5): p. 459-68.
3. Greenhalgh, E. and M.H. Garcia, *Fracture mechanisms and failure processes at stiffener run-outs in polymer matrix composite stiffened elements.* Composites Part A (Applied Science and Manufacturing), 2004. **35A**(12): p. 1447-58.
4. Hosseini-Toudeshky, H., et al., *Analysis of composite skin/stiffener debounding and failure under uniaxial loading.* Composite Structures, 2006. **75**(1-4): p. 428-436.
5. Mahdi, S., et al., The mechanical performance of repaired stiffened panels. Part II. Finite element modelling. Composites Part B:Engineering, 2002. **33**(5): p. 355-366.
6. Krueger, R. and P.J. Minguet, Analysis of composite skin-stiffener debond specimens using a shell/3D modeling technique. Composite Structures, 2007. **81**(1): p. 41-59.
7. Falzon, B.G. and G.A.O. Davies, *The Behavior of Compressively Loaded Stiffener Run-out Specimens – Part I:Experiments.* Journal of composite materials, 2002. **37**(No. 5/2003).
8. Falzon, B.G. and D. Hitchings, The Behavior of Compressively Loaded Stiffener Run-out Specimens – Part II: Finite Element Analysis. Journal of composite materials, 2002. **37**(No. 5/2003).
9. Krueger, R., Virtual crack closure technique: history, approach and applications. Appl Mech Rev, 2004. **57:109–43**.
10. Bisagni, C., R. Vescovini, and C.G. Davila, *Assessment of the damage tolerance of postbuckled hat-stiffened panels using single-stringer specimens.* AIAA-2010-2696, 51st AIAA/ASME/ASCE/AHS/ASC Structures, Structural Dynamics, and Materials Conference, 2010.
11. Camanho, P.P., C.G. Davila, and S.T. Pinho, . *Fracture analysis of composite co-cured structural joints using decohesion elements.* Fatigue Fract Engng Mater struct 27, 2004: p. 745- 757.
12. Psarras, S., S.T. Pinho, and B.G. Falzon, *Design of composite stiffener run-outs for damage tolerance.* Finite Elements in Analysis and Design, 2011. **47**(8): p. 949-954.
13. Simulia, Rising Sun Mills, 166 Valley Street, Providence, RI 02909-2499, USA, ABAQUS 6.10, 2011.
14. Python, *Python Software Foundation (PSF).* Wolfeboro Falls, NH 03896-0037, PO Box 37, USA, Python 2.6.2, 2010.
15. Krueger, R., J.G. Ratcliffe, and P.J. Minguet, *Panel stiffener debonding analysis using a shell/3D modeling technique.* Composites Science and Technology, 2009. **69**(14): p. 2352-2362.
16. Benzeggagh, M.L. and M. Kenane, Measurement of mixed-mode delamination fracture toughness of unidirectional glass/epoxy composites with mixed-mode bending apparatus. Composites Science and Technology, 1996. **56**(4): p. 439-49.
17. Gutkin, R., et al., *On acoustic emission for failure investigation in CFRP.* Mechanical Systems and Signal Processing 25, 2011. **1393–1407**.